

1 **The effects of different footprint sizes and cloud algorithms on the**
2 **top-of-atmosphere radiative flux calculation from the Clouds and**
3 **Earth's Radiant Energy System (CERES) instrument on**
4 **Suomi-NPP**

5 WENYING SU, *

Science Directorate, NASA Langley Research Center, Hampton, Virginia

6 LUSHENG LIANG, WALTER F. MILLER, VICTOR E. SOTHCOTT

Science Systems & Applications, Inc., Hampton, Virginia

* *Corresponding author address:* Wenying Su, MS420, NASA Langley Research Center, Hampton, VA 23681.

E-mail: Wenying.Su-1@nasa.gov

ABSTRACT

7
8 Only one CERES instrument is onboard the Suomi-NPP and it has been placed in cross-track
9 mode since launch, it is thus not possible to construct a set of angular distribution models
10 (ADMs) specific for CERES on NPP. Edition 4 Aqua ADMs are used for flux inversions for
11 CERES-NPP measurements. However, the footprint size of CERES-NPP is greater than
12 that of CERES-Aqua, as the altitude of the NPP orbit is higher than that of the Aqua orbit.
13 Furthermore, cloud retrievals from the Visible Infrared Imaging Radiometer Suite (VIIRS)
14 and the Moderate Resolution Imaging Spectroradiometer (MODIS), the imagers fly along-
15 side CERES-NPP and CERES-Aqua, are also different. To quantify the flux uncertainties
16 due to the footprint size difference between CERES-Aqua and CERES-NPP, and due to both
17 the footprint size difference and cloud property difference, a simulation is designed using the
18 MODIS pixel level data which are convolved with the CERES-Aqua and CERES-NPP point
19 spread functions into their respective footprints. The simulation is designed to isolate the
20 effects of footprint size and cloud property differences on flux uncertainty from calibration
21 and orbital differences between CERES-NPP and CERES-Aqua. The footprint size differ-
22 ence between CERES-Aqua and CERES-NPP introduces instantaneous flux uncertainties in
23 monthly gridded CERES-NPP of less than 4.0 Wm^{-2} for SW, and less than 1.0 Wm^{-2} for
24 both daytime and nighttime LW. The global monthly mean instantaneous SW flux from sim-
25 ulated CERES-NPP has a low bias of 0.4 Wm^{-2} when compares to simulated CERES-Aqua,
26 and the root-mean-square (RMS) error is 2.2 Wm^{-2} between them; the biases of daytime
27 and nighttime LW flux are close to zero with RMS errors of 0.8 Wm^{-2} and 0.2 Wm^{-2} . These
28 uncertainties are within the uncertainties of CERES ADMs. When both footprint size and
29 cloud property (cloud fraction and optical depth) differences are considered, the uncertain-
30 ties of monthly gridded CERES-NPP SW flux can be up to 20 Wm^{-2} in the Arctic regions
31 where cloud optical depth retrievals from VIIRS differ significantly from MODIS. The global
32 monthly mean instantaneous SW flux from simulated CERES-NPP has a high bias of 1.1
33 Wm^{-2} and the RMS error increases to 5.2 Wm^{-2} . LW flux shows less sensitivity to cloud

34 property differences than SW flux, with the uncertainties of about 2 Wm^{-2} in monthly grid-
35 ded LW flux, and the RMS errors of global monthly mean daytime and nighttime fluxes
36 increase only slightly. These results highlight the importance of consistent cloud retrieval
37 algorithms to maintain the accuracy and stability of the CERES climate data record.

1. Introduction

The Clouds and Earth’s Radiant Energy System (CERES) project has been providing data products critical to advancing our understanding of the effects of clouds and aerosols on radiative energy within the Earth-atmosphere system. CERES data are used by the science community to study the Earth’s energy balance (e.g., Trenberth et al. 2009; Kato et al. 2011; Loeb et al. 2012; Stephens et al. 2012), aerosol direct radiative effects (e.g., Satheesh and Ramanathan 2000; Zhang et al. 2005; Loeb and Manalo-Smith 2005; Su et al. 2013), aerosol-cloud interactions (e.g., Loeb and Schuster 2008; Quaas et al. 2008; Su et al. 2010b), and to evaluate global general circulation models (e.g., Pincus et al. 2008; Su et al. 2010a; Wang and Su 2013; Wild et al. 2013).

Six CERES instruments have flown on four different satellites thus far. CERES pre-Flight Model (FM) on Tropical Rainfall Measuring Mission (TRMM) was launched on November 27, 1997 into a 350-km circular precessing orbit with a 35° inclination angle and flew together with the Visible and Infrared Scanner (VIRS). CERES instruments (FM1 and FM2) on Terra were launched on December 18, 1999 into a 705-km sun-synchronous orbit with a 10:30 a.m. equatorial crossing time. CERES instruments (FM3 and FM4) on Aqua satellite were launched on May 4, 2002 into a 705-km sun-synchronous orbit with a 1:30 p.m. equatorial crossing time. CERES on Terra and Aqua flies alongside Moderate-Resolution Imaging Spectroradiometer (MODIS). CERES instrument (FM5) was launched onboard Suomi-NPP (hereafter referred to as NPP) on October 28, 2011 into a 824-km sun-synchronous orbit with a 1:30 p.m. equatorial crossing time and flies alongside the Visible Infrared Imaging Radiometer Suite (VIIRS). As the orbit altitudes differ among these satellites, the spatial resolutions of CERES instruments also vary from each other. TRMM has the lowest orbit altitude and offers the highest spatial resolution of CERES measurements, about 10 km at nadir; the spatial resolution of CERES on Terra and Aqua is about 20 km at nadir; and is about 24 km at nadir for NPP as it has the highest orbit altitude.

The CERES instrument consists of a three-channel broadband scanning radiometer (Wielicki

65 et al. 1996). The scanning radiometer measures radiances in shortwave (SW, 0.3-5 μm), win-
 66 dow (WN, 8-12 μm), and total (0.3-200 μm) channels. The longwave (LW) component is
 67 derived as the difference between total and SW channels. These measured radiances (I) at
 68 a given sun-Earth-satellite geometry are converted to outgoing reflected solar and emitted
 69 thermal TOA radiative fluxes (F) as:

$$F(\theta_0) = \frac{\pi I(\theta_0, \theta, \phi)}{R_j(\theta_0, \theta, \phi)}. \quad (1)$$

70 where θ_0 is the solar zenith angle, θ is the CERES viewing zenith angle, ϕ is the relative
 71 azimuth angle between CERES and the solar plane, and $R_j(\theta_0, \theta, \phi)$ is the anisotropic factors
 72 for scene type j . Here scene type is a combination of variables (e.g., surface type, cloud
 73 fraction, cloud optical depth, cloud phase, aerosol optical depth, precipitable water, lapse
 74 rate, etc) that are used to group the data to develop distinct angular distribution models
 75 (ADMs). Note the SW ADMs are developed as a function of θ_0, θ, ϕ for each scene type,
 76 whereas the LW ADMs are a weak function of θ_0 and ϕ and are developed only as a function
 77 of θ (Loeb et al. 2005; Su et al. 2015a).

78 To facilitate the construction of ADMs, there are pairs of identical CERES instruments
 79 on both Terra and Aqua. At the beginning of these missions one of the instruments on each
 80 satellite was always placed in a rotating azimuth plane (RAP) scan mode, while the other
 81 one was placed in cross-track mode to provide spatial coverage. When in RAP mode, the
 82 instrument scans in elevation as it rotates in azimuth, thus acquiring radiance measurements
 83 from a wide range of viewing combinations. There are about 60 months of RAP data collected
 84 on Terra and about 32 months of RAP data collected on Aqua. CERES instruments fly
 85 alongside high-resolution imagers, which provide accurate scene type information within
 86 the CERES footprints. Cloud and aerosol retrievals based upon high-resolution imager
 87 measurements are averaged over the CERES footprints by accounting for the CERES point
 88 spread function (PSF, Smith 1994) and are used for scene type classification. Similarly,
 89 spectral radiances from MODIS/VIIRS observations are averaged over the CERES footprints
 90 weighted by the CERES PSF. Surface types are obtained from the International Geosphere

91 Biosphere Program (IGBP) global land cover data set. Fresh snow and sea ice surface
92 types are derived from a combination of the National Snow and Ice Data Center (NSIDC)
93 microwave snow/ice map and the National Environmental Satellite, Data and Information
94 Service (NESDIS) snow/ice map. NESDIS uses imager data to identify snow and sea ice
95 and provide snow and sea ice information near the coast, whereas NSIDC does not provide
96 microwave retrievals within 50 km of the coast.

97 TRMM ADMs were developed using 9 months of CERES observations and the scene
98 identification information retrieved from VIRS observations (Loeb et al. 2003). Terra ADMs
99 and Aqua ADMs were developed separately using multi-year CERES Terra and Aqua mea-
100 surements in RAP mode and in cross-track mode using the scene identification information
101 from Terra MODIS and Aqua MODIS (Loeb et al. 2005; Su et al. 2015a). The high-resolution
102 MODIS imager provides cloud conditions for every CERES footprint. The cloud algorithms
103 developed by the CERES cloud working group retrieve cloud fraction, cloud optical depth,
104 cloud phase, cloud top and effective temperature/pressure (among other variables) based on
105 MODIS pixel-level measurements (Minnis et al. 2010). These pixel-level cloud properties
106 are spatially and temporally matched with the CERES footprints and are used to select the
107 scene-dependent ADMs to convert the CERES measured radiances to fluxes (Eq.1). The
108 spatial matching criterion used is 1 km. The temporal matching criterion used is less than
109 20 seconds when CERES is in cross-track mode, and less than 6 minutes when CERES is in
110 RAP mode.

111 There is only one CERES instrument on NPP and it has been placed in cross-track scan
112 mode since launch, it is thus not feasible to develop a specific set of ADMs for CERES
113 on NPP. Currently, the Edition 4 Aqua ADMs (Su et al. 2015a) are used to invert fluxes
114 for the CERES measurements on NPP. The CERES footprint size on NPP is larger than
115 that on Aqua. As pointed out by Di Girolamo et al. (1998), the nonreciprocal behavior
116 of the radiation field depends on measurement resolution, which means the ADMs do too.
117 They concluded that ADMs should be applied only to data of the same resolution as the

118 data used to derive the ADMs. Since the footprint sizes are different between CERES-Aqua
119 and CERES-NPP, will using ADMs developed based upon CERES-Aqua measurements for
120 CERES-NPP flux inversion introduce any uncertainties in the CERES-NPP flux? Addition-
121 ally, ADMs are scene type dependent, it is important to use consistent scene identification
122 for developing and applying the ADMs. However, the VIIRS channels are not identical to
123 those of MODIS, especially the lack of $6.7 \mu\text{m}$ and $13.3 \mu\text{m}$ channels, caused the cloud prop-
124 erties retrieved from MODIS and VIIRS differ from each other. These differences affect the
125 scene identification used to select the ADMs for flux inversion and thus can lead to addi-
126 tional uncertainties in the CERES-NPP flux. In this study, we design a simulation study to
127 quantify the CERES-NPP flux uncertainties due to the footprint size difference alone, and
128 due to both the footprint size and cloud property differences.

129 **2. Comparison between CERES-Aqua and CERES-NPP**

130 Besides the altitude differences between Aqua and NPP satellites, they are also different
131 in other orbital characteristics. For example, the orbital period for Aqua is about 98.82
132 minutes, while it is about 101.44 minutes for NPP; and the orbital inclination for Aqua is
133 about 98.20° , while it is about 98.75° for NPP. These orbital differences result in different
134 local overpass times between Aqua and NPP and their orbits fly over each other about every
135 64 hours. These simultaneous observations from Aqua and NPP are matched to compare
136 SW and LW radiances using CERES Aqua Edition 4 Single Scanner Footprint TOA/Surface
137 Fluxes and Clouds (SSF) product and CERES NPP Edition 1 SSF product. Here we use I_a^m
138 to denote the CERES-Aqua (subscript a) measured (superscript m) radiance, and I_n^m as the
139 CERES-NPP (subscript n) measured radiance. Similarly, F_a^m and F_n^m are the fluxes derived
140 from I_a^m and I_n^m using CERES Aqua ADMs. The matching criteria used for SW radiances
141 are that the latitude and longitude differences between the Aqua footprints and the NPP
142 footprints are less than 0.05 degree, solar zenith angle and viewing zenith angle differences

143 are less than 2 degrees, and relative azimuth angle difference is less than 5 degrees. Same
144 latitude and longitude matching criteria are used for LW radiances and the viewing zenith
145 angle difference between the Aqua footprints and the NPP footprints is less than 2 degrees.

146 Figure 1 shows the SW, daytime LW, and nighttime LW radiance comparisons between
147 CERES-Aqua and CERES-NPP using matched footprints of 2013 and 2014. The total
148 number of matched footprints, the mean I_a^m and I_n^m , and the root-mean-square (RMS)
149 errors are summarized in Table 1. The mean SW I_n^m is about $1 \text{ Wm}^{-2}\text{sr}^{-1}$ greater than I_a^m ,
150 the mean daytime LW I_n^m is about $0.4 \text{ Wm}^{-2}\text{sr}^{-1}$ smaller than I_a^m , and the nighttime LW I_n^m
151 and I_a^m agree to within $0.1 \text{ Wm}^{-2}\text{sr}^{-1}$. These comparisons include data taken from nadir to
152 oblique viewing angles ($\theta > 60$). The RMS errors remain almost the same when we compare
153 the radiances taken at different θ ranges. Footprint size differences may also contribute to
154 the radiance differences, but these radiance differences should be random. It is likely that
155 the footprint size differences can increase the RMS errors, but the mean radiance differences
156 are mostly resulted from calibration differences between CERES-Aqua and CERES-NPP.
157 As mentioned earlier, the daytime CERES LW radiance is derived as the difference between
158 total channel and SW channel measurements, and the nighttime CERES LW radiance is
159 directly derived from the total channel measurements. The differences shown in Table 1
160 indicate that the agreement of the total channels between CERES-Aqua and CERES-NPP
161 are better than that of the SW channels, leading to a smaller daytime LW difference than SW
162 difference. Loeb et al. (2016) examined the normalized instrument gains for the total and
163 SW channels for CERES FM1-FM5 since the beginning of the mission (BOM). The total
164 channel response to LW radiation has gradually increased with time for all instruments.
165 For the two instruments (FM3 and FM5) that are of interest here, the increases relative to
166 the BOM are 0.7% for FM3 and 0.4% for FM5. The SW channel response increases about
167 0.4% for FM3 and decreases by 0.2% for FM5. Exact causes for the calibration differences
168 between CERES-Aqua and CERES-NPP are not yet known and more research are needed
169 to understand their differences. The future plan is to place CERES-NPP on the same

170 radiometric scale as CERES-Aqua.

171 Flux comparison using the same matched footprints are shown in Figure 2 and the mean
172 F_a^m and F_n^m , and the RMS errors between them are summarized in Table 1. Consistent with
173 the radiance comparisons, the mean SW F_n^m is about 3.8 Wm^{-2} greater than F_a^m , the mean
174 daytime LW F_n^m is about 1.0 Wm^{-2} smaller than F_a^m , and the mean nighttime LW F_n^m is
175 about 0.3 Wm^{-2} smaller than F_a^m . When we compare the relative RMS errors (RMS error
176 divided by the mean Aqua value) between radiance and flux, the relative flux RMS errors
177 (6.4% for SW, 2.2% for daytime LW, and 1.4% for nighttime LW) are always slightly larger
178 than the relative radiance RMS errors (6.0% for SW, 2.1% for daytime LW, and 1.1% for
179 nighttime LW). This indicates that additional uncertainties are added when the radiances
180 are converted to fluxes.

181 However, we cannot directly compare the gridded monthly mean fluxes from Aqua and
182 NPP as their overpass times differ. Figure 3 shows the monthly mean TOA solar insolation
183 difference between CERES-NPP and CERES-Aqua for April 2013. Solar insolation for NPP
184 overpass times are greater than that for Aqua overpass times over most regions, except
185 over the northern high latitude. Regional differences as large as 30 Wm^{-2} are observed
186 over the tropical regions and north of 60°N . Globally, the CERES-NPP monthly mean solar
187 insolation is greater than that of CERES-Aqua by 13.4 Wm^{-2} for this month. When we
188 compare the monthly gridded TOA reflected SW flux between CERES-NPP and CERES-
189 Aqua, most of the features resemble those of the insolation differences (not shown). We
190 thus compare the albedo between CERES-NPP and CERES-Aqua (Figure 4). Over most
191 regions, the albedo from CERES-NPP is greater than that from CERES-Aqua, except over
192 parts of tropical oceans and Antarctica where some negative differences are observed. The
193 global monthly mean albedo from CERES-NPP is greater than that from CERES-Aqua by
194 0.003 (1.02%). The albedo difference is mostly from the calibration differences (see Figure
195 1a), while the footprint size difference and scene identification difference also contribute to
196 the albedo difference.

197 The CERES cloud working group developed sophisticated cloud detection algorithms
198 using visible and infrared channels of MODIS separately for polar and non-polar regions
199 and for daytime, twilight, and nighttime (Trepte et al. 2010). However, these detection
200 algorithms have to be modified to apply to the VIIRS observations (Qing Trepte, personal
201 communication), as some of the MODIS channels utilized for cloud detection are not available
202 on VIIRS. These modifications include replacing the 2.1 μm MODIS channel with the 1.6
203 μm VIIRS channel, and replacing detection tests using MODIS 6.7 μm and 13.3 μm channels
204 with VIIRS 3.7 μm and 11 μm channels, and supplement with tests utilizing VIIRS 1.6 μm
205 channel and the brightness temperature differences between 11 μm and 12 μm . These changes
206 mainly affect the cloud detections over the polar regions. The parameterization of 1.24
207 μm reflectance were regenerated for VIIRS using improved wavelength and solar insolation
208 weighting, which affects cloud optical depth retrieval over the snow/ice surfaces (Szedung
209 Sun-Mack, personal communication). These changes result in different cloud properties
210 retrieved using MODIS and VIIRS, especially over the polar regions. Figure 5 shows the
211 daytime cloud fraction and cloud optical depth difference between VIIRS and Aqua-MODIS
212 for April 2013. Cloud fraction retrieved from VIIRS is greater than that from MODIS by
213 up to 10% and cloud optical depth from VIIRS is smaller than that from MODIS by 2~3
214 over part of the Antarctic. Cloud fraction from VIIRS over the northern high-latitude snow
215 regions is smaller than that from MODIS, while the optical depth from VIIRS is greater
216 than that from MODIS. Over the Arctic, cloud optical depth from VIIRS is much larger
217 than that from MODIS. Over the ocean between 60°S and 60°N, the differences in cloud
218 fraction seem rather random while the differences in cloud optical depth is mostly positive
219 (VIIRS retrieval is greater than Aqua-MODIS retrieval).

220 Given that the footprint sizes and overpass times are different between CERES-Aqua
221 and CERES-NPP, in addition to the calibration differences and cloud retrieval differences
222 between them, fluxes from these CERES instruments cannot be compared directly to assess
223 the effects of footprint size difference and cloud property difference on flux uncertainty.

3. Method

To quantify the footprint size and cloud retrieval effect on flux inversion without having to account for the calibration and overpass time differences, we design a simulation study using the MODIS pixel level data and the Aqua-Earth-Sun geometry. MODIS spectral measurements are used to retrieve cloud properties and aerosol optical depth. These pixel-level imager-derived aerosol and cloud properties, and spectral narrowband (NB) radiances from MODIS are convolved with the CERES PSF to provide the most accurate aerosol and cloud properties that are spatially and temporally matched with the CERES broadband radiance data. Figure 6 illustrates the process of generating the simulated CERES-Aqua and CERES-NPP footprints from the MODIS pixels. We first use the CERES-Aqua PSF to convolve the aerosol/cloud properties, and the MODIS NB radiances (and other ancillary data) into Aqua-size footprints (left portion of Figure 6), as is done for the standard CERES-Aqua SSF product. These NB radiances for the simulated CERES-Aqua footprints are denoted as $I_a^s(\lambda)$, where superscript ‘s’ is for the simulated (in contrast to superscript ‘m’ for the measured). We then increase the footprint size to be that of NPP and use the CERES-NPP PSF to average the MODIS NB radiances, cloud/aerosol properties, and other ancillary data into the simulated NPP footprints. NB radiances for the simulated CERES-NPP footprints are denoted as $I_n^s(\lambda)$.

The cloud properties in the simulated CERES-Aqua footprints and in the simulated CERES-NPP footprints are all based upon the MODIS retrievals, so the scene identifications used to select ADMs for flux inversion are almost the same for both the simulated CERES-Aqua and the CERES-NPP, except small differences due to differing footprint sizes. As demonstrated in Figure 5, cloud properties differ between the MODIS and the VIIRS retrievals. These cloud retrieval differences affect the anisotropy factors selected for flux inversion. To simulate both the footprint size and cloud property differences, cloud fraction and cloud optical depth retrievals from MODIS convolved in the simulated CERES-NPP footprints are adjusted to be similar to those from VIIRS retrievals to assess how cloud

251 retrieval differences affect the flux. To accomplish this, daily cloud fraction ratios of VIIRS
252 to MODIS are calculated for each 1° latitude by 1° longitude grid box. These ratios are then
253 applied to the cloudy footprints of MODIS retrieval to adjust the MODIS cloud fractions
254 to be nearly the same as those from VIIRS retrieval. Note no adjustment is done for clear
255 footprints. Similarly, daily cloud optical depth ratios of VIIRS to MODIS are calculated us-
256 ing cloudy footprints for each 1° by 1° grid box. These ratios are used to adjust the MODIS
257 retrieved cloud optical depth to be close to those from VIIRS retrievals. The process of gen-
258 erating the simulated CERES-NPP footprints with VIIRS-like cloud retrievals is illustrated
259 on the right side of Figure 6, and the NB radiances for these footprints are denoted as $I_a^s(\lambda)$

260 Four months (July 2012, October 2012, January 2013, and April 2013) of simulated
261 CERES-Aqua and CERES-NPP data were created. For every CERES-Aqua footprint, it
262 contains the broadband SW and LW radiances measured by the CERES instrument. The
263 simulated NPP footprints, however, do not contain broadband radiances. To circumvent
264 this issue, we developed narrowband-to-broadband coefficients to convert the MODIS NB
265 radiances to broadband radiances.

266 The Edition 4 CERES-Aqua SSF data from July 2002 to September 2007 are used to
267 derive the narrowband-to-broadband (NB2BB) regression coefficients separately for SW,
268 daytime LW, and nighttime LW. Seven MODIS spectral bands (0.47, 0.55, 0.65, 0.86, 1.24,
269 2.13, and $3.7 \mu\text{m}$) are used to derive the broadband SW radiances, and the SW regression
270 coefficients are calculated for every calendar month for discrete intervals of solar zenith angle,
271 viewing zenith angle, relative azimuth angle, surface type, snow/non-snow conditions, cloud
272 fraction, and cloud optical depth. Five MODIS spectral bands (6.7, 8.5, 11.0, 12.0, and 14.2
273 μm) are used to derive the broadband LW radiances, and the LW regression coefficients are
274 calculated for every calendar month for discrete intervals of viewing zenith angle, precipitable
275 water, surface type, snow/none-snow conditions, cloud fraction, and cloud optical depth. The
276 20 IGBP surface types are grouped into 8 surface types: ocean, forest, savanna, grassland,
277 dark desert, bright desert, the Greenland permanent snow, and the Antarctic permanent

278 snow. When there is sea ice over the ocean and snow over the land surface types, regression
 279 coefficients for ice and snow conditions are developed (only footprints with 100% sea ice/snow
 280 coverage are considered).

281 These SW and LW NB2BB regression coefficients are then applied to $I_a^s(\lambda)$, $I_n^s(\lambda)$, and
 282 $I_n^{\prime s}(\lambda)$ to derive the broadband radiances, I_a^s , I_n^s and $I_n^{\prime s}$, for simulated footprints of CERES-
 283 Aqua, CERES-NPP, and CERES-NPP with VIIRS-like clouds, shown on the left, middle,
 284 and right of Figure 6, if the footprint consists of a single surface type. As both simulated
 285 CERES-Aqua and CERES-NPP footprints use the Aqua-Earth-Sun geometry, I_a^s and I_n^s ($I_n^{\prime s}$)
 286 have the same Sun-viewing geometry. Even though the CERES-Aqua footprints contained
 287 the broadband radiances from CERES observations (I_a^m), we choose to use the broadband
 288 radiances calculated using the NB2BB regressions to ensure that I_a^s and I_n^s ($I_n^{\prime s}$) are consis-
 289 tently derived. Doing so we can isolate the flux differences between simulated CERES-Aqua
 290 and simulated CERES-NPP caused by footprint size difference (and cloud property differ-
 291 ence). Aqua ADMs are used to convert I_a^s , I_n^s , and $I_n^{\prime s}$ to fluxes, F_a^s , F_n^s , and $F_n^{\prime s}$, for the
 292 simulated CERES-Aqua and CERES-NPP footprints using the cloud properties retrieved
 293 from MODIS observations for scene type identification, and for the CERES-NPP footprints
 294 with VIIRS-like cloud properties.

295 4. Results

296 We first compare the footprint-level fluxes between simulated CERES-Aqua and simu-
 297 lated CERES-NPP using data of April 1, 2013 (about 700,000 footprints). As the cloud
 298 fraction and cloud optical depth adjustments are done at the grid box level, it is not feasible
 299 to compare footprint-level $F_a^{\prime s}$ and $F_n^{\prime s}$, and only footprint-level F_a^s and F_n^s are compared.
 300 For SW, the bias between F_a^s and F_n^s is 0.1 Wm^{-2} and the RMS error is 4.7 Wm^{-2} . For
 301 LW, the biases is close to zero and the RMS errors are 1.3 Wm^{-2} and 0.9 Wm^{-2} for daytime
 302 and nighttime, respectively. These flux RMS errors are much smaller than those listed in

303 Table 1, indicating that calibration differences are responsible for most of the flux differences
304 between CERES-Aqua and CERES-NPP measurements. However, we should avoid direct
305 comparisons between these two sets of RMS errors, as they are derived using different time
306 period.

307 We now compare the monthly grid box (1° latitude by 1° longitude) mean fluxes from the
308 three simulations outlined in the previous section. Differences between F_n^s and F_a^s are used
309 to assess the CERES-NPP gridded monthly mean instantaneous flux uncertainties due to the
310 footprint size difference, and differences between $F_n'^s$ and F_a^s are used to assess the CERES-
311 NPP gridded monthly mean instantaneous flux uncertainties due to both the footprint size
312 and cloud property differences.

313 The monthly mean instantaneous TOA SW fluxes for simulated CERES-Aqua (F_a^s) are
314 shown in Figure 7(a) for April 2013. Note these fluxes are different from those in the Edition
315 4 Aqua SSF product as the CERES measured radiances differ from those inferred using
316 NB2BB regression coefficients. The flux differences caused by the footprint size difference
317 between the simulated CERES-NPP and the simulated CERES-Aqua ($F_n^s - F_a^s$) are shown in
318 Figure 7(b). Grid boxes in white indicate that the number of footprints with valid SW fluxes
319 differ by more than 2% between simulated CERES-Aqua and CERES-NPP, as the NB2BB
320 regressions are only applied to footprints that consist of the same surface types which
321 result in fewer footprints with valid fluxes for CERES-NPP than for CERES-Aqua. The
322 footprint size difference between CERES-Aqua and CERES-NPP introduces an uncertainty
323 that rarely exceeds 4.0 Wm^{-2} in monthly gridded CERES-NPP instantaneous SW fluxes.
324 For global monthly mean instantaneous SW flux, the simulated CERES-NPP has a low bias
325 of 0.4 Wm^{-2} compared to the simulated CERES-Aqua, and the RMS error between them is
326 2.4 Wm^{-2} . Results from the other three months are very similar to April 2013 (not shown).

327 Figure 7(c) shows the SW flux difference caused by both the footprint size and cloud prop-
328 erty differences ($F_n'^s - F_a^s$). Adding the cloud property differences increase the CERES-NPP
329 flux uncertainty comparing to when only footprint size differences are considered (Figure

330 7(b)), monthly gridded instantaneous flux uncertainty over the Arctic ocean can exceed 20
331 Wm^{-2} . Accounting for cloud property differences, the global monthly mean instantaneous
332 SW flux from simulated CERES-NPP has a high bias of 1.1 Wm^{-2} and the RMS error is
333 increased to 5.2 Wm^{-2} . Over the Arctic Ocean, the cloud optical depth from VIIRS retrieval
334 is much greater than that from the MODIS retrieval while the difference in cloud fraction is
335 relatively small. Anisotropic factors for thick clouds are smaller than those for thin clouds
336 at oblique viewing angles, and are larger for near-nadir viewing angles. The viewing ge-
337 ometries over the Arctic Ocean produced more smaller anisotropic factors than larger ones
338 when MODIS cloud optical depths were replaced with VIIRS-like cloud optical depths, which
339 resulted in larger fluxes when using VIIRS-like cloud properties for flux inversion.

340 The daytime and nighttime LW flux from the simulated CERES-Aqua footprints, LW
341 flux differences due to footprint size difference, and LW flux difference due to both footprint
342 size difference and cloud property difference are shown in Figures 8 and 9. The effect of
343 footprint size on gridded monthly mean daytime and nighttime LW flux is generally within
344 1.0 Wm^{-2} . For global monthly mean LW flux, the differences between $F_n^s - F_a^s$ are close to
345 zero, and the RMS errors between them are about 0.8 Wm^{-2} and 0.2 Wm^{-2} for daytime
346 and nighttime LW fluxes. When cloud property differences are also considered, their effect
347 on gridded monthly mean LW fluxes increases to about 2 Wm^{-2} . The RMS errors of global
348 monthly mean LW flux increase slightly to about 0.9 Wm^{-2} and 0.5 Wm^{-2} for daytime and
349 nighttime. The LW fluxes showed much less sensitivity to cloud property changes than the
350 SW fluxes, especially over the Arctic Ocean where cloud optical depth changed significantly.
351 This is because the LW ADMs over the snow/ice surfaces have very little sensitivity to cloud
352 optical depth (Su et al. 2015a), but they were developed for discrete cloud fraction intervals
353 and larger flux changes are noted in regions experiencing large cloud fraction changes.

5. Summary and discussion

The scene-type dependent ADMs are used to convert the radiances measured by the CERES instruments to fluxes. Specific empirical ADMs were developed for CERES instruments on TRMM, Terra, and Aqua (Loeb et al. 2003, 2005; Su et al. 2015a). As there is only one CERES instrument on NPP and it has been placed in cross-track mode since launch, it is not possible to construct a set of ADMs specific for CERES on NPP. Edition 4 Aqua ADMs (Su et al. 2015a) are thus used for flux inversions for CERES-NPP measurements. However, the altitude of the NPP orbit is higher than that of the Aqua orbit resulting in a larger CERES footprint size on NPP than on Aqua. Given that the footprint size of CERES-NPP is different from that of CERES-Aqua, we need to quantify the CERES-NPP flux uncertainty caused by using the CERES-Aqua ADMs. Furthermore, there are some differences between the imagers fly alongside CERES-Aqua (MODIS) and CERES-NPP (VIIRS), as VIIRS lacks the $6.7 \mu\text{m}$ and $13.3 \mu\text{m}$ channels. These spectral differences and algorithm differences lead to notable cloud fraction and cloud optical depth differences retrieved from MODIS and VIIRS. As the anisotropy factors are scene-type dependent, differences in cloud properties will also introduce uncertainties in flux inversion. Furthermore, the calibrations between CERES instruments on Aqua and on NPP also are different from each other. Comparisons using two years of collocated CERES-Aqua and CERES-NPP footprints indicate that the SW radiances from CERES-NPP are about 1.5% greater than those from CERES-Aqua, the daytime LW radiances from CERES-NPP are about 0.5% smaller than those from CERES-Aqua, and the nighttime LW radiances agree to within 0.1%.

To quantify the flux uncertainties due to the footprint size difference between CERES-Aqua and CERES-NPP, and due to both the footprint size difference and cloud property difference, we use the MODIS pixel level data to simulate the CERES-Aqua and CERES-NPP footprints. The simulation is designed to isolate the effects of footprint size difference and cloud property difference on flux uncertainty from calibration difference between CERES-NPP and CERES-Aqua. The pixel-level MODIS spectral radiances, the imager-derived

381 aerosol and cloud properties, and other ancillary data are first convolved with the CERES
382 Aqua PSF to generate the simulated CERES-Aqua footprints, and then convolved with
383 the CERES NPP PSF to generate the simulated CERES-NPP footprints. Broadband radi-
384 ances within the simulated CERES-Aqua and CERES-NPP footprints are derived using the
385 MODIS spectral bands based upon narrowband-to-broadband regression coefficients devel-
386 oped using five-years of Aqua data to ensure consistency between broadband radiances from
387 simulated CERES-Aqua and CERES-NPP. These radiances are then converted to fluxes
388 using the CERES-Aqua ADMs. The footprint size difference between CERES-Aqua and
389 CERES-NPP introduces instantaneous flux uncertainties in monthly gridded CERES-NPP
390 of less than 4.0 Wm^{-2} for SW, and less than 1.0 Wm^{-2} for both daytime and nighttime
391 LW. The global monthly mean instantaneous SW flux from simulated CERES-NPP has a
392 low bias of 0.4 Wm^{-2} compares to that from simulated CERES-Aqua, and the RMS error
393 between them is 2.4 Wm^{-2} . The biases in global monthly mean LW fluxes are close to zero,
394 and the RMS errors between simulated CERES-NPP and simulated CERES-Aqua are about
395 0.8 Wm^{-2} and 0.2 Wm^{-2} for daytime and nighttime global monthly mean LW fluxes.

396 The cloud properties in the simulated CERES-Aqua footprints and in the simulated
397 CERES-NPP footprints are all based upon MODIS retrievals, but in reality cloud prop-
398 erties retrieved from VIIRS differ from those from MODIS. To assess the flux uncertainty
399 from scene identification differences, cloud fraction and cloud optical depth in the simulated
400 CERES-NPP footprints are perturbed to be more like the VIIRS retrievals. When both
401 footprint size and cloud property differences are considered, the uncertainties of monthly
402 gridded CERES-NPP SW flux can be up to 20 Wm^{-2} in the Arctic regions where cloud
403 optical depth retrievals from VIIRS differ significantly from MODIS. The global monthly
404 mean instantaneous SW flux from simulated CERES-NPP has a high bias of 1.1 Wm^{-2} and
405 the RMS error is increased to 5.2 Wm^{-2} . LW flux shows less sensitivity to cloud property
406 differences than SW flux, with the uncertainties of about 2.0 Wm^{-2} in monthly gridded LW
407 flux, and the RMS errors increases to 0.9 Wm^{-2} and 0.5 Wm^{-2} for daytime and nighttime

408 LW flux.

409 Su et al. (2015b) quantified the global monthly 24hr-averaged flux uncertainties due to
410 CERES ADMs using direct integration tests, and concluded that the RMS errors are less
411 than 1.1 Wm^{-2} and 0.8 Wm^{-2} for 24hr-averaged TOA SW and LW fluxes. The uncertainty
412 for global monthly instantaneous SW flux is approximately twice the uncertainty of 24hr-
413 averaged flux. This simulation study indicates that the footprint size differences between
414 CERES-NPP and CERES-Aqua introduce flux uncertainties that are within the uncertain-
415 ties of the CERES ADMs. However, the uncertainty assessment provided here should be
416 considered as the low end, as many regions (especially over land, snow, and ice) were not
417 included due to sample number differences within the grid boxes. When cloud property
418 differences are accounted for, the SW flux uncertainties increase significantly and exceed the
419 uncertainties of the CERES ADMs. These findings indicate that inverting CERES-NPP flux
420 using CERES-Aqua ADMs resulting in flux uncertainties that are within the ADMs uncer-
421 tainties as long as the cloud retrievals between VIIRS and MODIS are consistent. When
422 the cloud retrieval differences between VIIRS and MODIS are accounted for, the SW flux
423 uncertainties exceed those of the CERES ADMs. To maintain the consistency of the CERES
424 climate data record, it is thus important to develop cloud retrieval algorithms that account
425 for the capabilities of both MODIS and VIIRS to ensure consistent cloud properties from
426 both imagers.

427

428 *Acknowledgments.*

429 This research was supported by the NASA CERES project. The CERES data were ob-
430 tained from the NASA Langley Atmospheric Science Data Center at https://eosweb.larc.nasa.gov/project/ceres/ssf_table. We thank Norman Loeb, Szedung Sun-Mack, Qing Trepte, and
431 Patrick Minnis for helpful discussions, and the three reviewers for their constructive com-
432 ments and suggestions which have significantly improved this paper.

REFERENCES

- 436 Di Girolamo, L., T. Varnai, and R. Davies, 1998: Apparent breakdown of reciprocity in
437 reflected solar radiances. *J. Geophys. Res.*, **103 (D8)**, 8795–8803.
- 438 Kato, S., et al., 2011: Improvements of top-of-atmosphere and surface irradiance computa-
439 tion with CALIPSO-, and MODIS-derived cloud and aerosol properties. *J. Geophys. Res.*,
440 **116 (D19209)**, D19 209, doi:10.1029/2011JD016050.
- 441 Loeb, N. G., S. Kato, K. Loukachine, and N. Manalo-Smith, 2005: Angular distribution
442 models for top-of-atmosphere radiative flux estimation from the clouds and the earth’s
443 radiant energy system instrument on the terra satellite. part I: Methodology. *J. Atmos.*
444 *Oceanic Technol.*, **22**, 338–351.
- 445 Loeb, N. G., J. M. Lyman, G. C. Johnson, R. P. Allan, D. R. Doelling, T. Wong, B. J.
446 Soden, and G. L. Stephens, 2012: Observed changes in top-of-the-atmosphere radiation
447 and upper-ocean heating consistent within uncertainty. *Nature Geosci.*, **5**, 110–113, doi:
448 10.1038/NGEO1375.
- 449 Loeb, N. G. and N. Manalo-Smith, 2005: Top-of-atmosphere direct radiative effect of aerosols
450 over global oceans from merged CERES and MODIS observations. *J. Climate*, **18**, 3506–
451 3526.
- 452 Loeb, N. G., N. Manalo-Smith, S. Kato, W. F. Miller, S. K. Gupta, P. Minnis, and B. A.
453 Wielicki, 2003: Angular distribution models for top-of-atmosphere radiative flux estima-
454 tion from the Clouds and the Earth’s Radiant Energy System instrument on the Tropical
455 Rainfall Measuring Mission satellite. Part I: Methodology. *J. Appl. Meteor.*, **42**, 240–265.

- 456 Loeb, N. G., N. Manalo-Smith, W. Su, M. Shankar, and S. Thomas, 2016: CERES top-of-
457 atmosphere Earth radiation budget climate data record: Accounting for in-orbit changes
458 in instrument calibration. *Remote Sens.*, **8 (182)**, doi:10.3390/rs8030182.
- 459 Loeb, N. G. and G. L. Schuster, 2008: An observational study of the relationship between
460 cloud, aerosol and meteorology in broken low-level cloud conditions. *J. Geophys. Res.*,
461 **113 (D14214)**, D14 214, doi:10.1029/2007JD009763.
- 462 Minnis, P., et al., 2010: CERES Edition 3 cloud retrievals. *13th Conference on Atmospheric*
463 *Radiation*, Am. Meteorol. Soc., Oregon, Portland.
- 464 Pincus, R., C. P. Batstone, R. J. P. Hofmann, K. E. Taylor, and P. J. Glecker, 2008: Evalu-
465 ating the present-day simulation of clouds, precipitation, and radiation in climate models.
466 *J. Geophys. Res.*, **113 (D14209)**, D14 209, doi:10.1029/2007JD009334.
- 467 Quaas, J., O. Boucher, N. Bellouin, and S. Kinne, 2008: Satellite-based estimate of the
468 direct and indirect aerosol climate forcing. *J. Geophys. Res.*, **113 (D05204)**, D05 204,
469 doi:10.1029/2007JD008962.
- 470 Satheesh, S. K. and V. Ramanathan, 2000: Large differences in tropical aerosol forcing at
471 the top of the atmosphere and earth's surface. *Nature*, **405**, 60–63.
- 472 Smith, G. L., 1994: Effects of time response on the point spread function of a scanning
473 radiometer. *Appl. Opt.*, **33**, 7031–7037.
- 474 Stephens, G. L., et al., 2012: An update on Earth's energy balance in light of the latest
475 global observations. *Nature Geosci.*, **5**, 691–696, doi:10:1038/NNGEO1580.
- 476 Su, W., A. Bodas-Salcedo, K.-M. Xu, and T. P. Charlock, 2010a: Comparison of the trop-
477 ical radiative flux and cloud radiative effect profiles in a climate model with Clouds and
478 the Earth's Radiant Energy System (CERES) data. *J. Geophys. Res.*, **115 (D01105)**,
479 D01 105, doi:10.1029/2009JD012490.

- 480 Su, W., J. Corbett, Z. A. Eitzen, and L. Liang, 2015a: Next-generation angular distribution
481 models for top-of-atmosphere radiative flux calculation from the CERES instruments:
482 Methodology. *Atmos. Meas. Tech.*, **8**, 611–632, doi:10.5194/amt-8-611-2015.
- 483 Su, W., J. Corbett, Z. A. Eitzen, and L. Liang, 2015b: Next-generation angular distribution
484 models for top-of-atmosphere radiative flux calculation from the CERES instruments:
485 Validation. *Atmos. Meas. Tech.*, **8**, 3297–3313, doi:10.5194/amt-8-3297-2015.
- 486 Su, W., N. G. Loeb, G. L. Schuster, M. Chin, and F. G. Rose, 2013: Global all-sky shortwave
487 direct radiative forcing of anthropogenic aerosols from combined satellite observations and
488 GOCART simulations. *J. Geophys. Res.*, **118**, 1–15, doi:10.1029/2012JD018294.
- 489 Su, W., N. G. Loeb, K. Xu, G. L. Schuster, and Z. A. Eitzen, 2010b: An estimate of aerosol
490 indirect effect from satellite measurements with concurrent meteorological analysis. *J.*
491 *Geophys. Res.*, **115 (D18219)**, D18 219, doi:10.1029/2010JD013948.
- 492 Trenberth, K. E., J. T. Fasullo, and J. Kiehl, 2009: Earth’s global energy budget. *Bull. Am.*
493 *Meteor. Soc.*, **90**, 311–323, doi:10.1175/2008BAMS2634.1.
- 494 Trepte, Q. Z., P. Minnis, C. Trepte, and S. Sun-Mack, 2010: Improved cloud detections in
495 CERES Edition 3 algorithm and comparison with the CALIPSO vertical feature mask.
496 *13th Conference on Atmospheric Radiation*, Am. Meteorol. Soc., Oregon, Portland.
- 497 Wang, H. and W. Su, 2013: Evaluating and understanding top of the atmosphere cloud
498 radiative effects in Intergovernmental Panel on Climate Change (IPCC) fifth assessment
499 report (AR5) clouded model intercomparison project phase 5 (CMIP5) models using
500 satellite observations. *J. Geophys. Res.*, **118**, 1–17, doi:10.1029/2012JD018619.
- 501 Wielicki, B. A., B. R. Barkstrom, E. F. Harrison, R. B. Lee, G. L. Smith, and J. E. Cooper,
502 1996: Clouds and the Earth’s Radiant Energy System (CERES): An Earth Observing
503 System experiment. *Bull. Amer. Meteor. Soc.*, **77**, 853–868.

- 504 Wild, M., D. Folini, C. Schar, N. G. Loeb, E. G. Dutton, and G. Konig-Langlo, 2013:
505 The global energy balance from a surface perspective. *Clim. Dyn.*, **40**, 3107–3134, doi:
506 10.1007/s00382-012-1569-8.
- 507 Zhang, J., S. A. Christopher, L. A. Remer, and Y. J. Kaufman, 2005: Shortwave aerosol
508 radiative forcing over cloud-free oceans from Terra: 2. Seasonal and global distributions.
509 *J. Geophys. Res.*, **110 (D10S24)**, D10S24, doi:10.1029/2004JD005009.

510 **List of Tables**

511 1 Comparison of CERES-Aqua and CERES-NPP measured SW, daytime LW,
512 and nighttime LW radiances ($\text{Wm}^{-2}\text{sr}^{-1}$) and fluxes (Wm^{-2}) using matched
513 footprints of 2013 and 2014. 23

TABLE 1. Comparison of CERES-Aqua and CERES-NPP measured SW, daytime LW, and nighttime LW radiances ($\text{Wm}^{-2}\text{sr}^{-1}$) and fluxes (Wm^{-2}) using matched footprints of 2013 and 2014.

	SW	Daytime LW	Nighttime LW
Sample Number	147894	192178	187880
Mean CERES-Aqua Radiance	68.1	77.4	74.4
Mean CERES-NPP Radiance	69.2	77.0	74.3
Radiance RMS Error	4.1	1.6	0.8
Mean CERES-Aqua Flux	230.1	235.7	226.4
Mean CERES-NPP Flux	233.9	234.7	226.1
Flux RMS Error	14.6	5.0	3.1

514 List of Figures

- 515 1 Radiance comparisons between matched CERES-Aqua and CERES-NPP foot-
516 prints, (a) SW; (b) daytime LW; and (c) nighttime LW using data of 2013
517 and 2014. 26
- 518 2 Flux comparisons between matched CERES-Aqua and CERES-NPP foot-
519 prints, (a) SW; (b) daytime LW; and (c) nighttime LW using data of 2013
520 and 2014. 27
- 521 3 Monthly mean solar insolation difference (Wm^{-2}) between CERES-NPP and
522 CERES-Aqua (NPP-Aqua) for April 2013. 28
- 523 4 Monthly mean albedo difference between CERES-NPP and CERES-Aqua
524 (NPP-Aqua) for April 2013. 29
- 525 5 Cloud fraction (a) and cloud optical depth (b) differences between VIIRS and
526 MODIS (VIIRS-MODIS) retrievals for April 2013. 30
- 527 6 Schematic diagram of convoluting the MODIS pixels into the simulated Aqua
528 and NPP footprints. Left depicts the processes involved in producing the
529 simulated Aqua footprints; middle for simulated NPP footprints with MODIS
530 retrievals; and right for simulated NPP footprints with VIIRS-like retrievals. 31
- 531 7 The gridded monthly mean TOA instantaneous SW fluxes from the simulated
532 Aqua footprints (F_a^s , a), the flux differences caused by footprint size difference
533 between simulated NPP and simulated Aqua ($F_n^s - F_a^s$, b), and the flux differ-
534 ences caused by both footprint size and cloud property differences ($F_n'^s - F_a^s$,
535 c) using April 2013 data. Regions shown in white have large sample number
536 differences between simulated Aqua and simulated NPP. 32

- 537 8 The gridded monthly mean TOA daytime LW fluxes from the simulated Aqua
538 footprints (F_a^s , a), the flux differences caused by footprint size difference be-
539 tween simulated NPP and simulated Aqua ($F_n^s - F_a^s$, b), and the flux differ-
540 ences caused by both footprint size and cloud property differences ($F_n'^s - F_a^s$,
541 c) using April 2013 data. Regions shown in white have large sample number
542 differences between simulated Aqua and simulated NPP. 33
- 543 9 The gridded monthly mean TOA nighttime LW fluxes from the simulated
544 Aqua footprints (F_a^s , a), the flux differences caused by footprint size difference
545 between simulated NPP and simulated Aqua ($F_n^s - F_a^s$, b), and the flux differ-
546 ences caused by both footprint size and cloud property differences ($F_n'^s - F_a^s$,
547 c) using April 2013 data. Regions shown in white have large sample number
548 differences between simulated Aqua and simulated NPP. 34

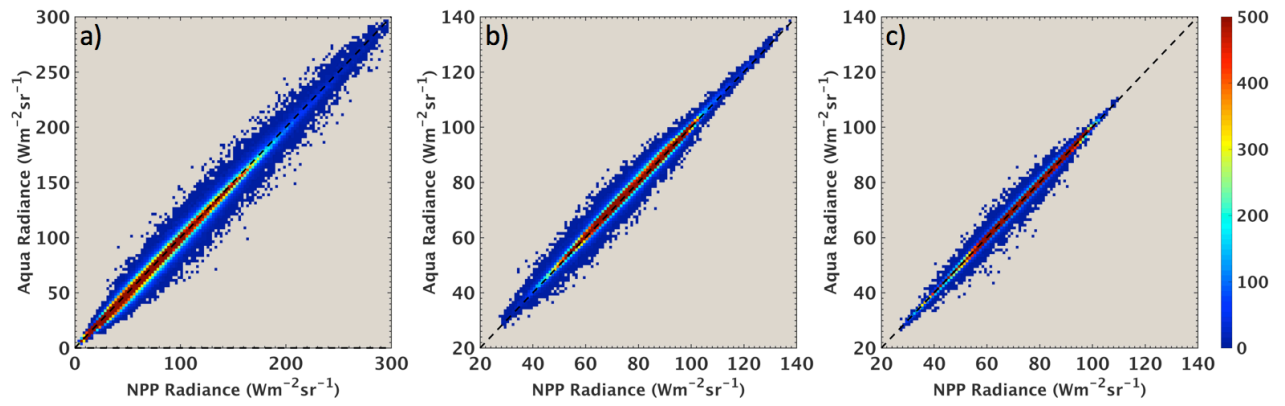


FIG. 1. Radiance comparisons between matched CERES-Aqua and CERES-NPP footprints, (a) SW; (b) daytime LW; and (c) nighttime LW using data of 2013 and 2014.

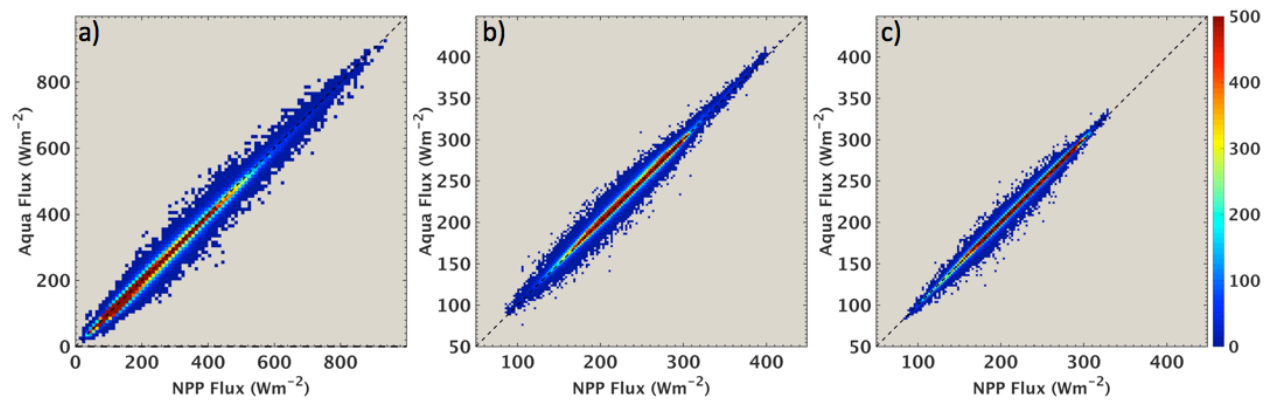


FIG. 2. Flux comparisons between matched CERES-Aqua and CERES-NPP footprints, (a) SW; (b) daytime LW; and (c) nighttime LW using data of 2013 and 2014.

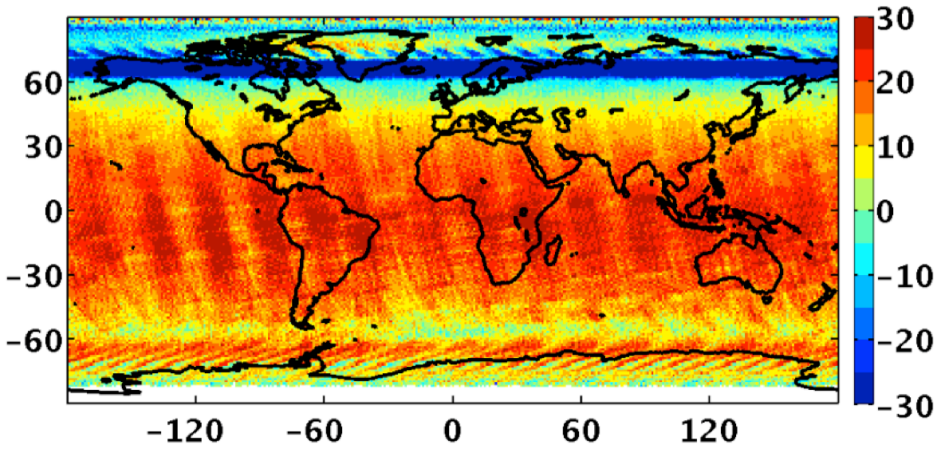


FIG. 3. Monthly mean solar insolation difference (Wm^{-2}) between CERES-NPP and CERES-Aqua (NPP-Aqua) for April 2013.

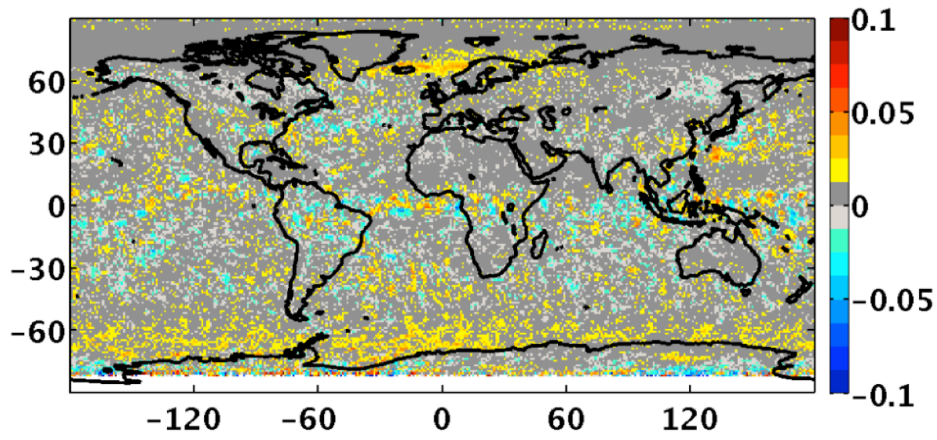


FIG. 4. Monthly mean albedo difference between CERES-NPP and CERES-Aqua (NPP-Aqua) for April 2013.

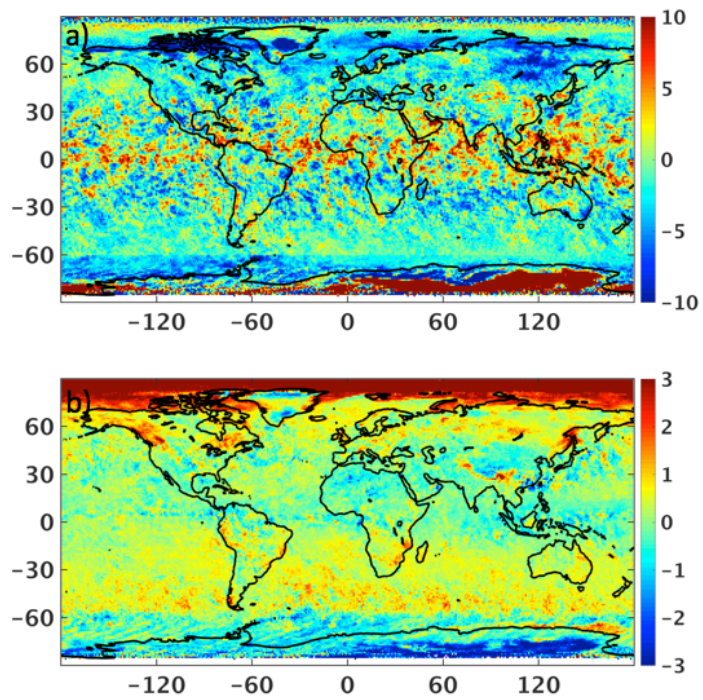


FIG. 5. Cloud fraction (a) and cloud optical depth (b) differences between VIIRS and MODIS (VIIRS-MODIS) retrievals for April 2013.

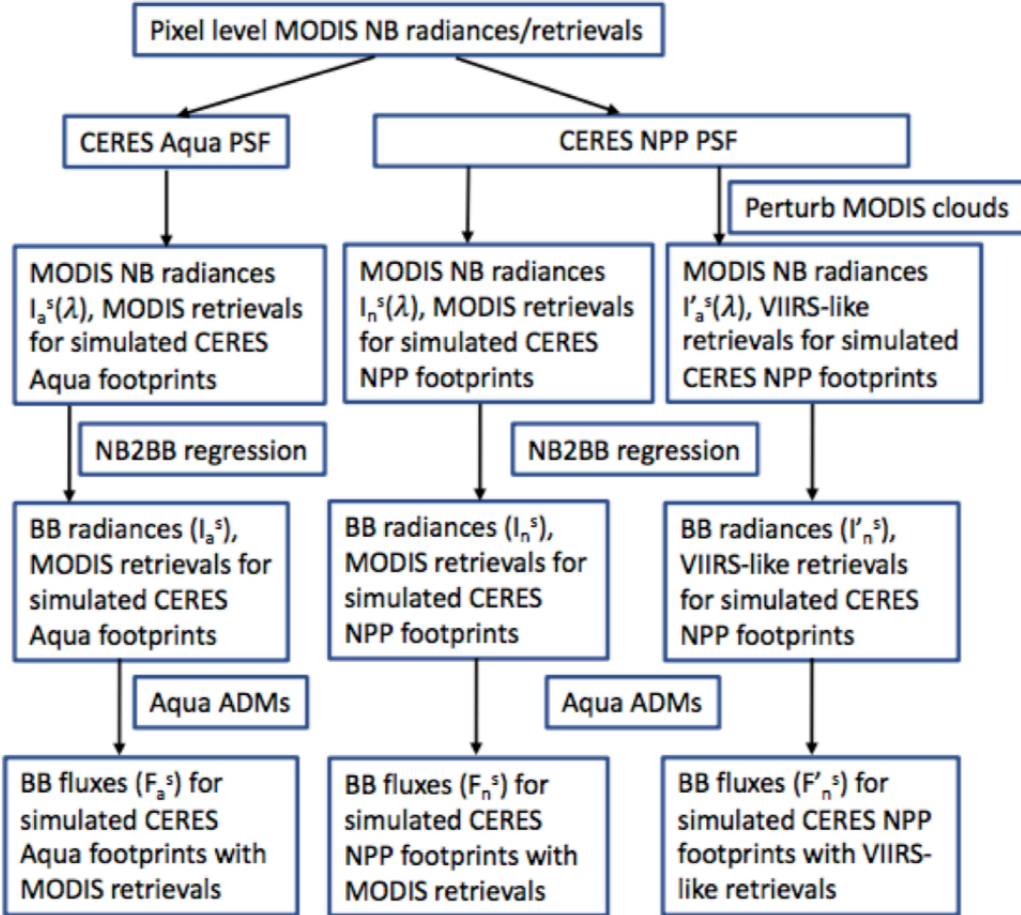


FIG. 6. Schematic diagram of convoluting the MODIS pixels into the simulated Aqua and NPP footprints. Left depicts the processes involved in producing the simulated Aqua footprints; middle for simulated NPP footprints with MODIS retrievals; and right for simulated NPP footprints with VIIRS-like retrievals.

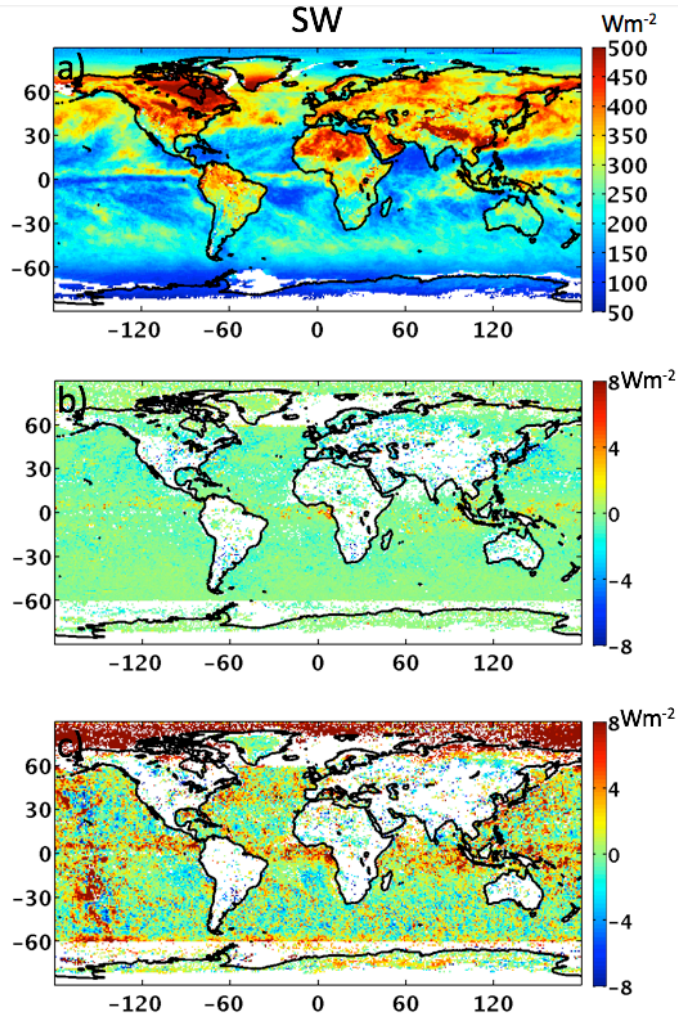


FIG. 7. The gridded monthly mean TOA instantaneous SW fluxes from the simulated Aqua footprints (F_a^s , a), the flux differences caused by footprint size difference between simulated NPP and simulated Aqua ($F_n^s - F_a^s$, b), and the flux differences caused by both footprint size and cloud property differences ($F_n'^s - F_a^s$, c) using April 2013 data. Regions shown in white have large sample number differences between simulated Aqua and simulated NPP.

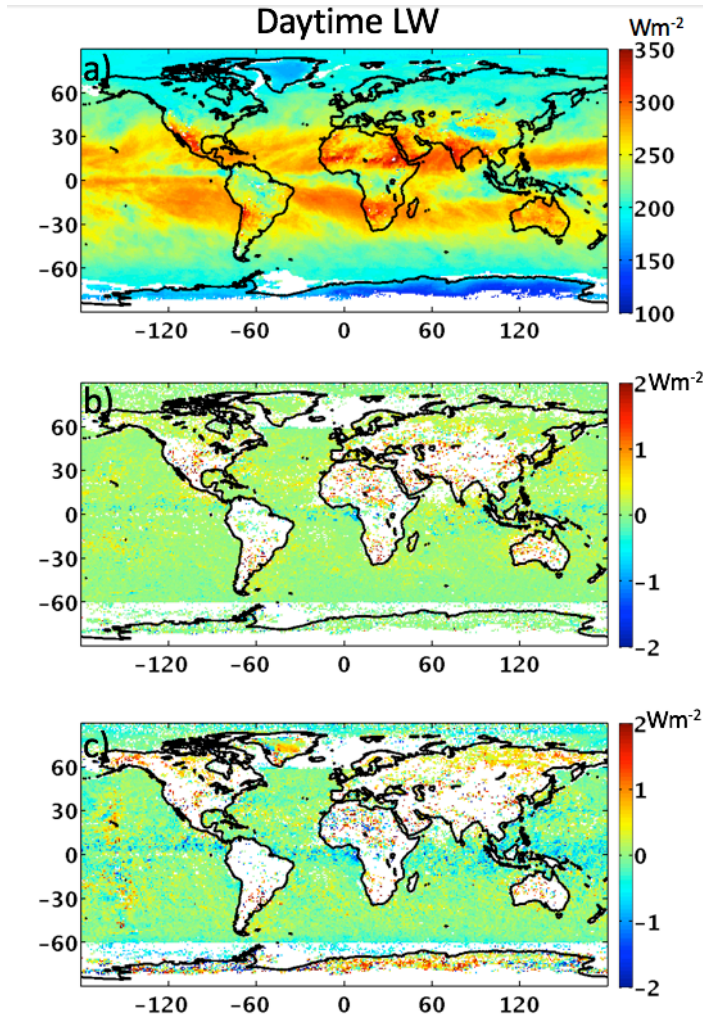


FIG. 8. The gridded monthly mean TOA daytime LW fluxes from the simulated Aqua footprints (F_a^s , a), the flux differences caused by footprint size difference between simulated NPP and simulated Aqua ($F_n^s - F_a^s$, b), and the flux differences caused by both footprint size and cloud property differences ($F_n'^s - F_a^s$, c) using April 2013 data. Regions shown in white have large sample number differences between simulated Aqua and simulated NPP.

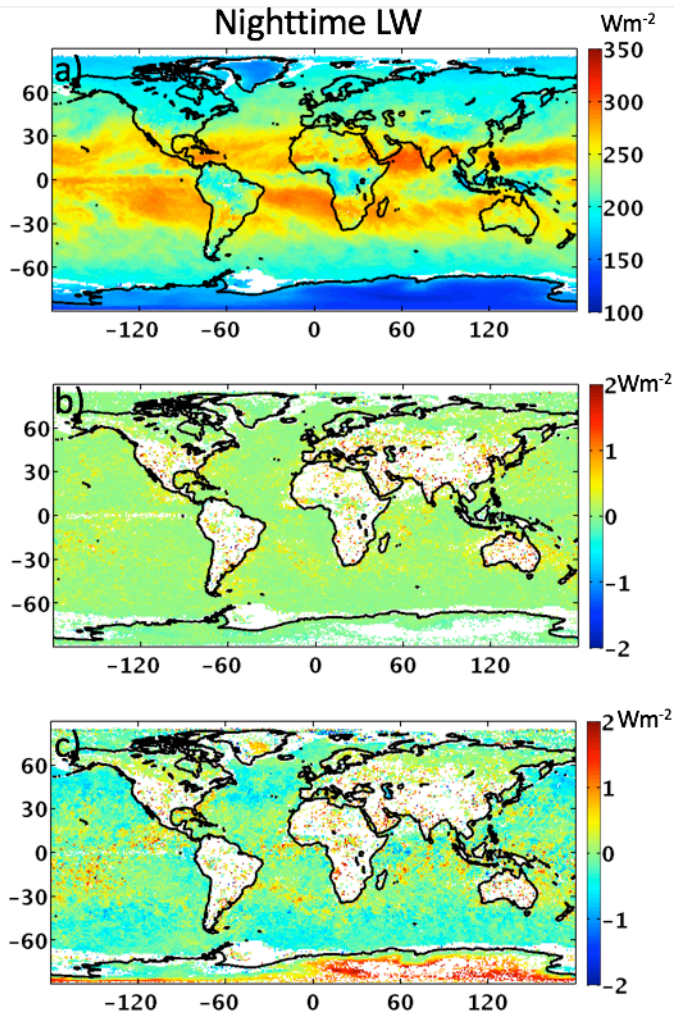


FIG. 9. The gridded monthly mean TOA nighttime LW fluxes from the simulated Aqua footprints (F_a^s , a), the flux differences caused by footprint size difference between simulated NPP and simulated Aqua ($F_n^s - F_a^s$, b), and the flux differences caused by both footprint size and cloud property differences ($F_n'^s - F_a^s$, c) using April 2013 data. Regions shown in white have large sample number differences between simulated Aqua and simulated NPP.